An Inductive Monitoring Method Leveraging Tunable Mixing Phase Difference for Wear Debris Inspection

Guan Wang[1], Zhenghua Qian[1,2]*, Dianzi Liu [3,4]*, Peng Li[1,2], Tianhao Xie[1], Iren Kuznetsova[5]

(1.Nanjing University of Aeronautics and Astronautics, State Key Laboratory of Mechanics and Control for Aerospace Structures, Nanjing, 210016, China;

2.Shenzhen Research Institute, Nanjing University of Aeronautics and Astronautics, Shenzhen, 518057, China;

3.Research Center for Applied Mechanics, Xidian University, Xi'an 710071, China;

4.School of Engineering, Mathematics and Physics, University of East Anglia, Norwich, UK, NR4 7TJ

5.Nikov Institute of Radio Engineering and Electronics of RAS, Moscow 125009, Russia)

*** Corresponding author1**
*Name:***Zhenghua Qian**
*Author affiliation:*Nanjing University of Aeronautics and Astronautics, State Key Laboratory of Mechanics and Control for Aerospace Structures, Nanjing, 210016
*E-mail address:*qianzh@nuaa.edu.cn(Zhenghua Qian)

*** Corresponding author2**
Name: **Dianzi Liu**
*Author affiliation:*School of Engineering, University of East Anglia, Norwich, UK
*E-mail address:*dianzi.liu@uea.ac.uk(Dianzi Liu)

Abstract: In order to improve the feasibility and accuracy of inductive oil debris monitoring method for metal debris, lock-in amplifier (LIA) technology integrated with two digital frequency synthesizers is developed to enhance the wear monitoring capability of an inductive sensor under different Mixing Phase Difference (MPD). This new method leverages two adjustable digital synthesis chips to generate both an excitation signal and a square wave reference signal, therefore improving the signal-to-noise ratio (SNR) of debris signals. Moreover, with adjusting the MPD, variations in debris signal amplitude across different material types are examined in this study. Experimental results reveal substantial distinctions are achieved by determining the optimal MPD among different debris materials. Taking copper debris as an example, an appropriate adjustment increases the signal amplitude by as much as 3.48 times, demonstrating the remarkable sensitivity enhancement enabled by the approach. As a result, the proposed method is capable of effectively detecting iron debris as small as 80μm and copper debris down to 200μm in a piping system containing 13-mm diameter pipes.
Keywords: Inductive debris sensor, LIA technique, Reference signal adjustment, MPD adjustment, SNR improvement

1. Introduction

Large-scale power equipment operates under high loads and harsh conditions, which cause significant wear to transmission components[1-4].The lubrication system in such equipment not only reduces friction and seals components but also carries wear debris from bearings and gears out of the system through oil flow[5-7].Studies show that wear debris generated from direct abrasive damage or accelerated wear of contacting surfaces (such as gears and bearings), typically have diameters in the range of 20μm to 200μm. When a large number of debris exceeding 200μm are present[8], it usually indicates severe wear, and the equipment should be shut down for maintenance. Therefore, analyzing the quantity and size of debris provides valuable insights for assessing equipment health. Therefore, debris in the range of 20 to 200μm are the focal debris in this research and considered in the lubricant debris monitoring for mechanical fault diagnosis. Therefore, analyzing the quantity and size of debris provides valuable insights for assessing equipment health[9]. Thus, oil debris monitoring is essential for machinery fault diagnosis and maintenance[10-13].

Metal debris detections is generally classified into offline[14, 15] and online condition monitoring[16, 17]. Offline detection technologies have limitations for engineering applications due to their long cycle, high cost, and lack of real-time monitoring capability[18, 19]. In contrast, online monitoring methods provide real-time data about the size and concentration of metal debris by analyzing their effects on the physical properties of lubricating oil. Based on detection principles, online monitoring methods include, optical[20, 21], capacitance[22-24], ultrasonic[25, 26], resistance[27], and induction techniques[28].

The earliest inductive debris sensors were featured with a single-coil structure, first introduced by Flanagan[29], who established the fundamental principle of inductive detection for metallic wear debris. Li et al.[30] developed an induction pulse sensor with a planar coil structure, demonstrating the feasibility of planar designs for the improved detection resolution. This sensor utilized a glass tube with a 1mm inner diameter and was capable of detecting ferromagnetic debris larger than 50μm and non-ferromagnetic debris larger than 105μm in oil flow. Ma et al. [31] proposed a method to estimate debris composition and size and analyzed the influence of debris on the inductance and impedance signals of coils. They established, for the first time, a correlation model between coil inductive/impedance signals and debris composition and size, enabling both qualitative identification of debris materials and quantitative debris size detection. This work advanced inductive sensors from the application for single-parameter detection to multi-parameter characterization identification. Their system achieved detection of iron debris as small as 20μm and copper debris of 60μm in diameter within a 500μm diameter tube. Zeng et al.[32]enhanced the detection sensitivity of a dual-solenoid coil sensor by optimizing the number and configuration of silicon steel sheets. This optimal design improved the magnetic field distribution, significantly increasing the sensitivity for small-sized debris and lowering the detection limits for both ferromagnetic and non-ferromagnetic debris. Such sensor was capable of detecting iron debris as small as 33μm and copper debris larger than 90μm in a 0.9mm diameter tube. Shen et al.[33]further optimized the ratio of coil length to the number of turns through orthogonal experiments and coherent demodulation techniques. The developed approach reduced the radial position error in debris detection and improved the SNR, providing valuable guidance for sensor structure and demodulation optimization. The optimal design achieved detection of 93.5μm iron debris and 447.3μm copper debris in a 3mm diameter pipeline, with simulation results confirming that the radial position error was maintained below 5%.

The above studies have significantly advanced inductive debris sensing technology from the principle of verification toward sensor structure optimization, signal demodulation enhancement to multi-parameter characterization, with continuous improvements in debris detection sensitivity. However, most existing systems still rely on narrow-diameter flow channels to maintain detection sensitivity, which limits their engineering application for high-flow lubrication systems. In addition, research on the signal demodulation mechanism of debris remains relatively insufficient, resulting in relatively weak detection capability for non-ferromagnetic debris [34]. Studies have shown that ferromagnetic debris (e.g., iron) significantly increases the coil inductance in an external magnetic field, whereas diamagnetic materials (e.g., copper) resist magnetization and reduce coil inductance[35]. However, the inductive method is significantly more sensitive to ferromagnetic debris than to other types of magnetic debris. With advances in materials science, fabrications of bearings, gears, and other lubricated components are no longer limited to ferromagnetic materials, and the use of copper-based[36], aluminum-based[37, 38], and non-metallic materials[39] has become increasingly popular. In typical bearing tribosystems, the inner ring, outer ring, and rolling elements are manufactured from high-hardness bearing steel with excellent wear resistance. In contrast, critical sliding components including copper alloy cages, bronze thrust washers, and copper-based bearing shells, are widely used to form hard–soft steel–copper tribopairs[40, 41]. Due to their lower hardness and superior plastic deformation capacity, copper alloys are more susceptible to wear under sliding friction[42]. Therefore, enhancing the detection capability for diamagnetic debris is of great significance.

Inductive online monitoring methods typically distinguish material types based on debris signal phase and estimate debris size using the signal amplitude. However, conventional methods suffer from low sensitivity to diamagnetic debris and the limited capability in detecting small-sized non-ferromagnetic debris. Moreover, most existing inductive debris sensors employ narrow-diameter pipelines to improve detection resolution, which restricts the lubricant flow and limits their practical industrial applications. To address these limitations, this work develops a square-wave demodulation scheme based on a programmable digital frequency synthesizer. Thus, the influence of the MPD on the detection response of different metallic debris is systematically investigated, achieving good monitoring sensitivity for debris with different magnetic properties even under relatively large-diameter pipeline conditions. Compared with conventional debris-signal demodulation methods, this study demonstrates that the phase difference between the reference signal and the debris-induced signal should be determined according to the specific properties of the target metal being monitored, rather than being uniformly adjusted to zero as commonly adopted in previous studies. By optimizing the phase difference based on the characteristics of different metallic debris, the proposed method enhances the detection sensitivity for non-ferromagnetic debris and addresses a limitation of existing demodulation approaches. This finding provides a new perspective for improving the performance of inductive wear-debris monitoring systems. The proposed method enables the reliable detection of iron debris as small as 80μm in a 13mm diameter pipeline and copper debris down to 200μm, with the corresponding sensitivity factors S of 162.5 and 65, respectively. These factors are significantly higher than those obtained by conventional methods. Thus, the detection capability for diamagnetic debris is enhanced, thereby improving the feasibility and accuracy of oil debris monitoring technology.

2. Introduction to the Lock-In Amplifier Method

2.1. Sensor Structure

The most common configuration for inductive monitoring sensors is the three-coil structure, which consists of two excitation coils and one induction coil. The structural schematic and the parameter model is shown in Figure 1.

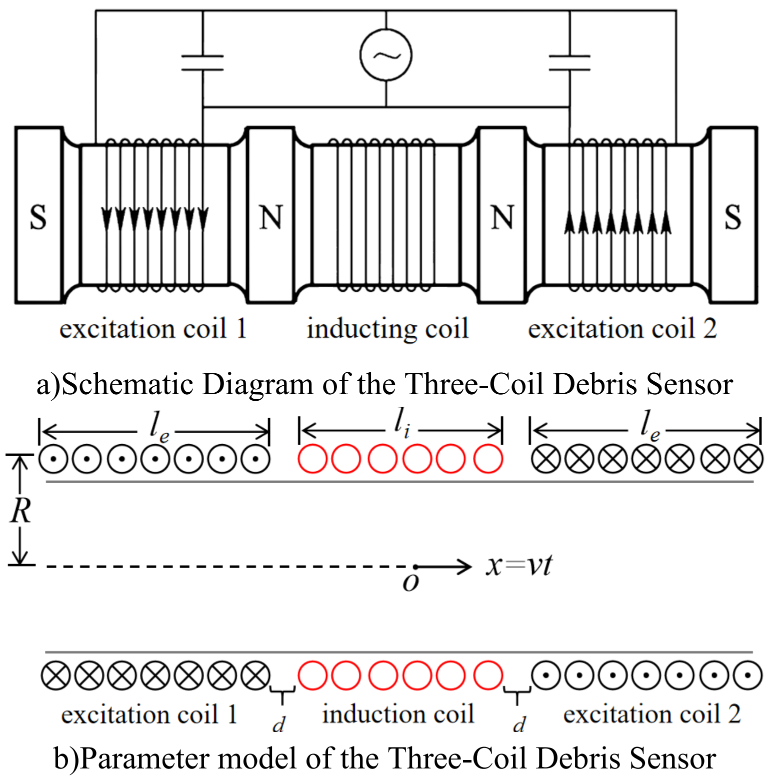

Figure 1. Schematic Diagram and parameter model of the Three-Coil Debris Sensor

In Figure 1, l_e and l_i represent the lengths of the excitation coil and the induction coil, respectively; d is the spacing between the coils; O denotes the origin of the coordinate system; and x means the axial position of the debris and is determined by the product of velocity v and time t. The sensor utilizes two excitation coils to establish a stable magnetic field. These coils are identical in material composition, length, and spacing, and are wound around a ceramic framework. They are connected in a reverse-parallel configuration to a common AC current source to ensure magnetic field symmetry. An induction coil placed at the center of the sensor aims for detection of variations in the magnetic field when debris passes through the sensor.

When the excitation coil set is energized with an alternating current of angular frequency omega, a time-varying magnetic flux density $B(x,t)$ is generated along the axial direction, which can be expressed as Eq. 1.

$$B(x,t) = B_L(x,t) + B_R(x,t) = Ie^{j\omega t}Ge(x) \tag{1}$$

where B_L and B_R denote the magnetic fields generated by the left and right excitation coils shown in Figure 1, respectively. I represents the amplitude of the excitation current, and ω means the angular frequency of the excitation current. $Ge(x)$ represents the geometric function of the excitation coil set, which is determined by the structural parameters of the excitation coils. The magnetic fields produced by the left and right excitation coils, B_L and B_R, are given by Eq. 2.

$$B_L(x,t)=\frac{\mu_0 n_e I(t)}{2}\left[\frac{x-x_{cL}+l_e/2}{\sqrt{R_e^2+\left(x-x_{cL}+l_e/2\right)^2}}-\frac{x-x_{cL}-l_e/2}{\sqrt{R_e^2+\left(x-x_{cL}-l_e/2\right)^2}}\right]$$
$$B_R(x,t)=\frac{\mu_0 n_e I(t)}{2}\left[\frac{x-x_{cR}-l_e/2}{\sqrt{R_e^2+\left(x-x_{cR}-l_e/2\right)^2}}-\frac{x-x_{cR}+l_e/2}{\sqrt{R_e^2+\left(x-x_{cR}+l_e/2\right)^2}}\right] \quad (2)$$

Where B_{cL} and B_{cR} represent the axial center positions of the left and right excitation coils, respectively. n_e represents the number of turns per unit length of the excitation coil, R_e is the radius of the excitation coil and μ_0 depicts the permeability of free space. When a spherical metallic debris with radius r_a enters the excitation magnetic field region of the sensor, it becomes magnetized under the applied alternating magnetic field. Since r_a is much smaller than the coil radius R, the magnetized debris can be approximated as a magnetic dipole, accordingly, it's magnetic dipole moment **m** is expressed as Eq. 3[43].

$$\mathbf{m}=\frac{4\pi}{3}r_a^3\chi_a\frac{B}{\mu_0} \quad (3)$$

In Eq. 3, χ_a denotes the complex magnetic susceptibility of the metallic debris, which is expressed as Eq. 4[44].

$$\chi_a=|\chi_a|e^{j\angle\chi_a} \quad (4)$$

The phase angle $\angle\chi_a$ represents the phase shift of the magnetic susceptibility, characterizing the time delay between the magnetization response of the debris and the applied alternating magnetic field.

Under the excitation magnetic field, the magnetized metallic debris behaves as a magnetic dipole, and the magnetic field generated by the dipole at an arbitrary spatial point p is referred to as the magnetic dipole field, which can be expressed as Eq. 5[45].

$$B_p=\frac{\mu_0}{4\pi}\frac{3(\mathbf{m}\cdot\vec{\mathbf{r}})\vec{\mathbf{r}}-\mathbf{m}}{r^3} \quad (5)$$

In this equation, r denotes the distance between the magnetic dipole and the spatial point p, and $\vec{\mathbf{r}}$ is the unit vector pointing from the dipole to the observation point. The total magnetic flux Φ induced in the induction coil by the magnetic dipole field can be regarded as the superposition of the magnetic flux through each turn of the coil. When the number of turns is sufficiently large, Φ can be approximated by Eq. 6

$$\Phi(x,t)=|\mathbf{m}(x,t)|\cdot Gi(x)=\frac{4\pi r_a^3\chi}{3\mu_0}I(t)Ge(x)Gi(x) \quad (6)$$

where $Gi(x)$ represents the geometric function of the induction coil, which depends on the structural parameters of the induction coil set and is given by Eq. 7.

$$Gi(x)=\frac{\mu_0 n_i}{2}\left[\frac{x+l_i/2}{\sqrt{R_i^2+(x+l_i/2)^2}}-\frac{x-l_i/2}{\sqrt{R_i^2+(x-l_i/2)^2}}\right] \tag{7}$$

In Eq. 7, n_i represents the number of turns per unit length of the induction coil and R_i means the radius of the induction coil.According to Faraday's law of electromagnetic induction, the induced electromotive force $\varepsilon(t)$ is given by:

$$\varepsilon(t)=-\frac{4\pi r_a^3\chi}{3\mu_0}Ie^{j\omega t}\left[j\omega Ge(x)Gi(x)+Ge^{'}(x)Gi(x)v+Ge(x)Gi^{'}(x)v\right] \tag{8}$$

By substituting the axial motion of the debris $x=vt$ and applying the chain rule, the induced electromotive force can be derived as shown in Eq. 8. An analysis of Eq. 8 indicates that the term $j\omega Ge(x)Gi(x)$ is approximately 4-5 orders of magnitude larger than the terms $Ge'(x)Gi(x)v$ and $Ge(x)Gi'(x)v$. Therefore, after incorporating the magnetic permeability, the real-valued electrical signal received by the induction coil can be approximated by Eq. 9.

$$\begin{aligned}\Re\left[\varepsilon(t)\right]&\approx\Re\left[-\frac{4\pi r_a^3\chi}{3\mu_0}Ie^{j\omega t}j\omega Ge(x)Gi(x)\right]\\&=-\frac{4\pi r_a^3|\chi|I\omega}{3\mu_0}G_e(x)G_i(x)\sin\left(\omega t+\angle\chi_a\right)\\&=A(t)\sin(2\pi f_e t+\angle\chi_a)\end{aligned} \tag{9}$$

where f_e denotes the excitation signal frequency.From the perspective of the overall sensor design, when metallic debris enters the induction region, it perturbs the originally stable magnetic field, thereby superimposing a disturbance onto the excitation signal. This interaction results in an amplitude-modulated output signal. Consequently, the electrical signal received by the induction coil can be regarded as a sinusoidally modulated signal, whose modulation envelope is determined by the debris properties as well as the geometric functions of the excitation and induction coils and is denoted as $A(t)$. In addition, the output induced signal is phase-shifted by $\angle\chi_a$ with respect to the excitation signal.

2.2. Overview of Debris Signal Demodulation Methods

Due to the small size of metal debris, the amplitudes of induced signals are typically in the microvolt range. Thus, the measurement accuracy is highly susceptible to mechanical vibration and system noise, which limits the effectiveness and broad applications of conventional frequency filters.

The LIA technique is specifically designed to extract weak signals from noisy environments. In recent years, researchers have implemented LIA using various approaches, including analog circuits[46], FPGA architectures[47], and digital signal processing [48]. These developments have significantly enhanced signal extraction capability, thereby enabling more reliable detection of weak sensor signals. The LIA and its deployment in the circuit are shown in Figure 2:

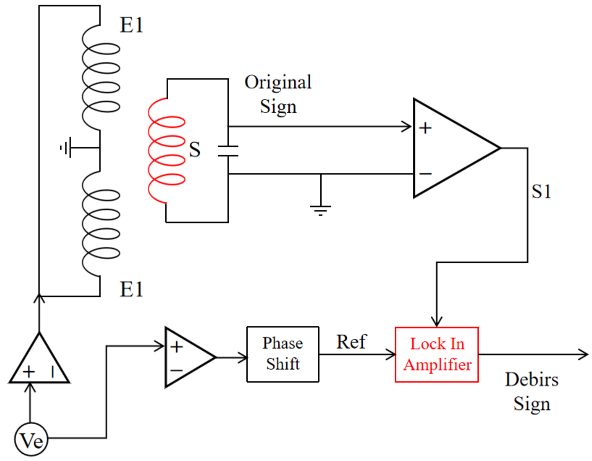

Figure 2. Schematic of the LIA in the whole circuit for processing debris signals

There are three steps described in the LIA for processing debris signals:

(1)Signal Generation: The sensor circuit generates a high-frequency signal, splitting it into two sub-signals. One is amplified to serve as the sensor's excitation voltage, while the other acts as a reference signal. Upon excitation, the sensor outputs a raw signal containing debris information.

(2)Phase Adjustment: The raw signal is amplified to obtain the signal S1 in Figure 2, and a phase-shifting circuit adjusts the reference signal to align with S1, During this adjustment process, the phase difference between the reference signal and S1 is defined as the MPD.

(3)Signal Mixing: The phase-aligned S1 and reference signals processed by LIA are converted into a mixed signal. Thus, the high-frequency carrier and noise are shifted to higher frequencies, which are removed by a low-pass filter for the isolation of the debris signal.

It should be noted that the adjustment process of the MPD occurs when the sensor is in a steady state, i.e., when no debris is passing through. Due to the presence of $\angle\chi_a$ in Eq. 9, even when MPD=0, there will still be a phase difference between the amplitude-modulated signal generated by the debris passing through the sensor and the reference signal.

Although widely used in debris signal demodulation, traditional LIA methods encounter several challenges. One major challenge is that the reference signal phase adjustment requires phase-shifting circuits. A typical phase-shifting circuit is depicted in Figure 3 as follows:

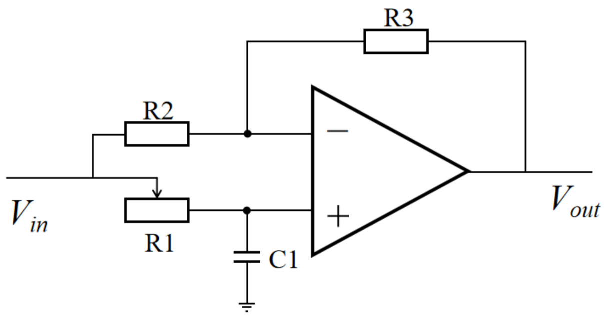

Figure 3. Schematic of the phase-shifting circuit

where the adjusting resistor R1 alters the input signal phase by a theoretical maximum shift of 90°. Usually, to attain a specific phase shift, multiple phase-shifting circuits in series are required, which complicates the LIA implementation.

To ensure that the excitation coil generates a stable magnetic field, the excitation signal is set as a single-frequency signal, specifically a sine wave. In Figure 2, both the excitation signal and the reference signal are derived from the same source, which also means that the reference signal is a sine wave. However, research has shown that when a square wave is used as the reference signal, the demodulated signal amplitude is highest. Assuming sine wave, square wave, and triangular wave are used as reference signals, with a phase φ_r and an amplitude A_r, the sine wave reference signal $r_s(t)$ is defined as:

$$r_s(t) = A_r \sin(2\pi f_e t + \varphi_r) \tag{10}$$

The Fourier series expansions of the squarer wave $r_q(t)$ and triangular wave $r_t(t)$ signals can be expressed as follows:

$$r_q(t) = \frac{4A_r}{\pi} \sum_{n=1,3,5,...}^{\infty} \frac{1}{n} \sin(2n\pi f_e t + n\varphi_r) \tag{11}$$

$$r_t(t) = \frac{8A}{\pi^2} \sum_{n=1,3,5,...}^{\infty} \frac{(-1)^{(n-1)/2}}{n^2} \sin(2n\pi ft + n\varphi_r) \tag{12}$$

After mixing the debris signal with the one shown in Eq. 9 and performing low-pass filtering, the resulting signals *Ms*, *Mq*, and *Mt* are expressed as:

$$\begin{aligned} Ms &= A_r A(t)\cos(\angle\chi_a - \varphi_r)/2 \\ Mq &= 2A_r A(t)\cos(\angle\chi_a - \varphi_r)/\pi \\ Mt &= 4A_r A(t)\cos(\angle\chi_a - \varphi_r)/\pi^2 \end{aligned} \tag{13}$$

Eq. 13 indicates two results. First, when the phase of the reference signal aligns with the phase of the debris's magnetic susceptibility, the demodulated signal amplitude is highest. When the phase difference is π, the signal amplitude takes the opposite sign. When the phase difference is π/4 or 5π/4, the signal amplitude becomes zero. Second, the type of reference signal used in the demodulation process affects the demodulated signal. Using a sine wave reference as the baseline, amplitudes of the signals demodulated using triangular and square wave as references are observed approximately 81.06% and 123.37% of the result obtained using the baseline, respectively.

3. Dual-Chip Excitation circuit design

In traditional oil debris monitoring systems, the phase of the reference signal is typically set to be in phase with the steady-state sensor signal S1, i.e., MPD=0[33]. As indicated by Eq. 4, Eq. 9, and Eq. 13, the magnetic susceptibility phases of debris vary with the material, requiring different optimal reference phases. By adjusting the MPD parameter based on the material type of the oil debris, the circuit can achieve maximum signal response. Meanwhile, using square waves as reference signals for debris signal demodulation further enhances the performance, significantly improving oil debris monitoring.

However, conventional circuits are typically designed to process sine waves, as the excitation and reference signals are usually generated from a common source. To overcome this limitation, this study proposes a signal demodulation circuit based on Dual-Chip Excitation (DCE), in which two independently controlled signal generators are controlled by a microcontroller unit (MCU) to enable square wave demodulation. By adjusting the MPD value, the system facilitates the analysis of signal amplitudes generated by debris of different materials under various MPD conditions.

The AD9833 chip communicates via the Serial Peripheral Interface (SPI), allowing multiple chips to share common clock and data lines while interfacing with a MCU. Chip Select lines are used to determine which chip is active for data reading or writing. This configuration enables the cooperation of two AD9833 chips using only four signal lines. It is worth noting that this observation could be extended to control n chips using just n+2 data lines. Meanwhile, all AD9833 chips should share the same external crystal oscillator (XO) to ensure clock synchronization. The schematic of the circuit configuration is shown in in Figure 4, and the sensor circuit using the DCE system is illustrated in Figure 5.

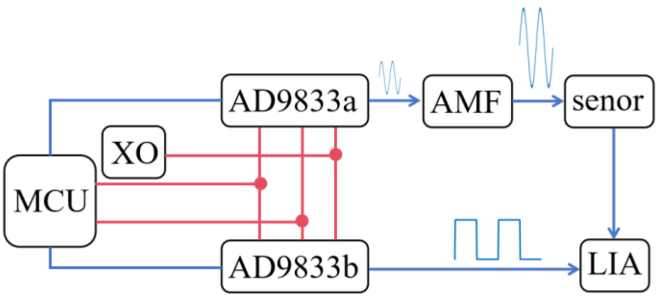

Figure 4. Schematic Diagram of the DCE Method

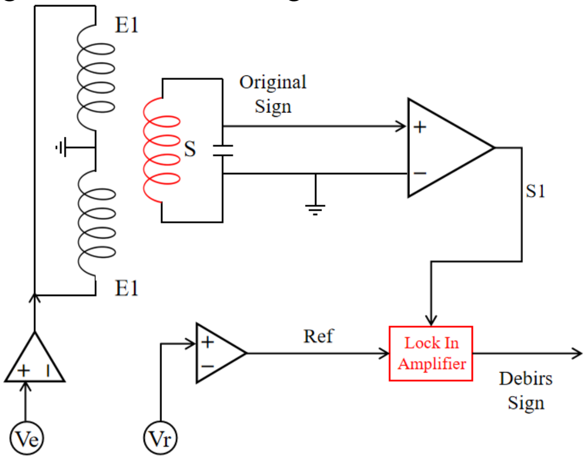

Figure 5. Schematic of the LIA in the whole circuit for processing debris signals base on DCE

As illustrated in Figure 4, the circuit integrates two AD9833 chips. Under the control of the MCU, AD9833-a generates an 80 kHz sine wave, which is subsequently amplified and applied as the excitation signal for the sensor. Simultaneously, AD9833-b produces an 80 kHz square wave that serves as the reference signal. This reference signal, along with the output from the sensor, is fed into a mixer. Following that, the mixed signal is then passed through a low-pass filter to extract the debris signal.

This circuit enables software-based control over the characteristics (frequencies phase, amplitude, and waveform) of excitation and reference signals, demonstrating the following advantages:

(1) Controlling the initial phase of the reference signal through MCU code enhances signal stability and simplifies phase adjustment, while also enabling external control via buttons or upper computer software.

(2) Facilitating the controllable square wave demodulation, which enhances the amplitude of the extracted debris signal.

(3) Elimination of complex analog phase adjustment, leading to a more streamlined circuit layout, reduction of the overall system cost, and lower susceptibility to noise interference.

4. Experimental Platform Configuration

4.1. Sensor Structure

The inductive oil debris sensor used in the experiment adopts a three-coil design, the sensor consists of two excitation coils and one receiving coil, each with a width of 10mm. The coils are arranged horizontally in the order of excitation coil 1, receiving coil, and excitation coil 2. All coils have an inner diameter of 13mm and an outer diameter of 16mm, with a spacing of 5mm between adjacent coils. Each coil is wound using 0.24mm coated copper wire, comprising four winding layers with a total of 80 turns. The resistance and inductance of each coil are approximately 3.5Ω and 340μH, respectively. These coils are identical in material composition, length, and spacing, and are wound around a ceramic framework. They are connected in a reverse-parallel configuration to a common AC current source to ensure magnetic field symmetry. An induction coil placed at the center of the sensor aims for detection of variations in the magnetic field when debris passes through the sensor. The entire coil assembly is enclosed within a metal housing for electromagnetic shielding, as depicted in Figure 6:

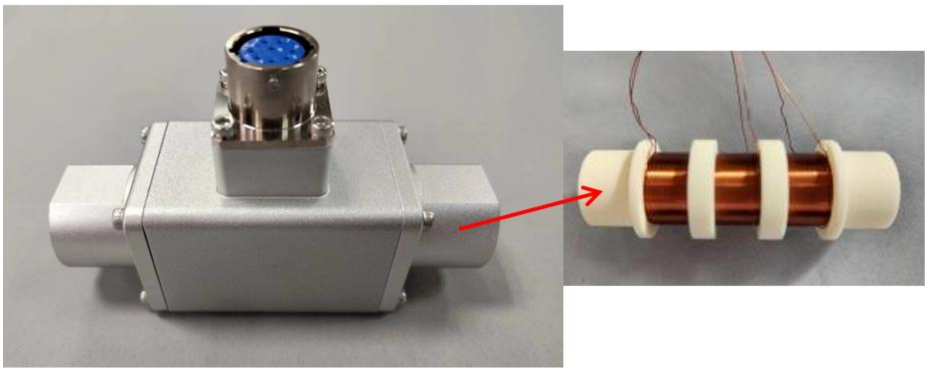

Figure 6. Schematic Diagram of the Framework and Housing

An 80 kHz sine wave as the input of the sensor is initially amplified to 25 V and used to drive the sensor. At the output, the sensor generates a signal at the microvolt level. A two-stage amplification circuit increases the signal by a factor of approximately 10,000 before it is passed to the mixer, where demodulation is performed using an 80 kHz square wave as a reference signal. After demodulation, a fourth-order Butterworth low-pass filter is applied to eliminate the carrier signal and suppress most of the noise.

The proposed sensor exhibits a fast response characteristic, and no observable delay is detected between debris passage and signal output. When the spatial distance between two debris exceeds 25mm, their signals can be fully separated. In the continuous measurement experiments, a spacing of 300mm was used between consecutive debris to ensure that no signal overlap occurs.

4.2. Experimental Platform Setup

To facilitate equipment debugging and accurately simulate debris movement in oil flow, an experimental platform was designed for debris detection. First, prefabricated debris is attached to a transmission rope using insulating tape. A motor is then employed to drive the rope, causing the debris to pass through the induction region of the sensor. Finally, the output signal by the sensor is captured and recorded by an oscilloscope. Compared with a real lubricating oil circulation system, the rope-driven apparatus has certain limitations, particularly in its inability to reproduce the stochastic motion of wear debris in turbulent oil flow. In addition, it does not capture the morphological diversity of real debris. Nevertheless, this experimental setup offers a short testing cycle, supports repeated high-throughput measurements, and enables debris recycling, thereby ensuring good experimental consistency despite its simplified configuration. The schematic and physical layout of the experimental platform are presented in Figure 7 and Figure 8:

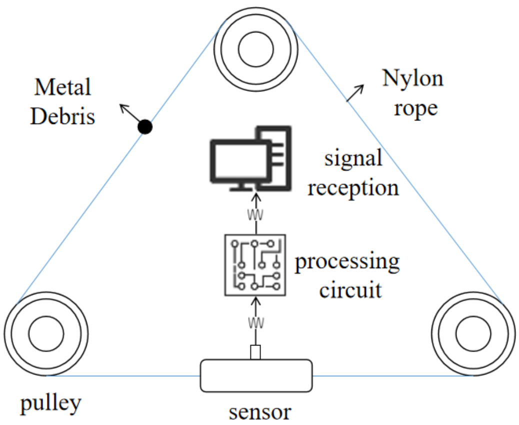

Figure 7. Schematic diagram of the experimental platform

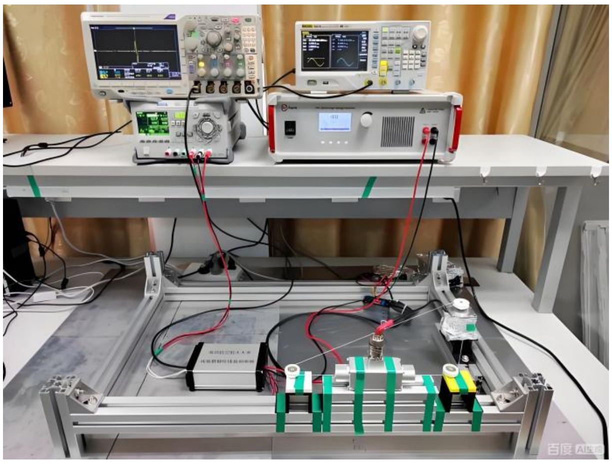

Figure 8. Experimental and testing platform

The transmission rope is made of nylon, whose magnetic permeability is close to that of air, thereby minimizing its influence on the sensor's internal magnetic field. Moreover, nylon exhibits good elasticity and moderate damping characteristics, which reduce the likelihood of slippage when the rope moves over the pulley. The debris is fabricated in a spherical shape, and its diameter is precisely measured and recorded under a microscope for subsequent analysis.

5. Debris Data Analysis

In this section, the developed apparatus initially examines the effectiveness of square-wave demodulation, and then conducts a comparative analysis of the signal amplitudes of debris made from different materials under various MPD values. Finally, quantitative analysis on the sensitivity of the sensor is performed. In all experiments, the sensor diameter selected is 13mm, and the baseline noise amplitude is controlled at the magnitude of 1mV using post-amplification. Each test was repeated multiple times, and the data were statistically analyzed. The coefficient of variation(CV) was introduced to evaluate data dispersion. The CV is formulated by Eq. 14.

$$\mathrm{CV} = SD / \bar{A} \tag{14}$$

where SD refers to the standard deviation of repeated measured data, and $\bar{A}$ is the average signal amplitude. A lower CV value reflects weaker data dispersion.

5.1. Comparative Study on Square Wave Demodulation

To assess the practical performance of the square-wave demodulation technique, the DCE method is employed to generate square, sine, and triangular waveform reference signals. In conjunction with the conventional phase adjustment method, these reference signals are utilized to compare the induced signals produced by 200μm iron debris. During the experiments, the MPD value is set to zero. The debris signals are illustrated in Figure 9:

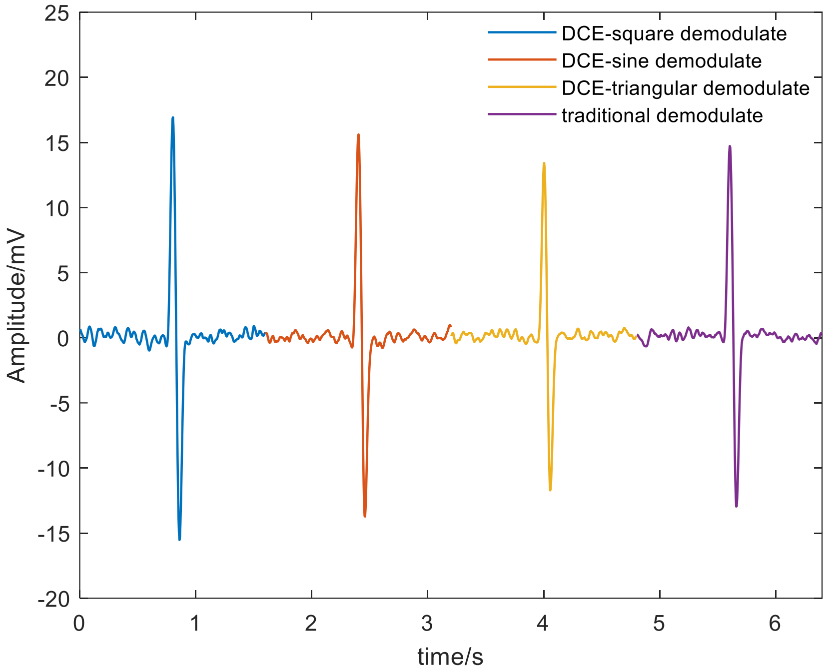

Figure 9. Comparison of Debris Signals from different demodulation methods

It can be observed that the square wave reference signal produces the highest amplitude of peak-to-peak values (Vpp), while the triangular wave results in the lowest Vpp. The traditional phase-shifting method yields a signal amplitude in between those by sinusoidal and triangular wave demodulations, indicating that the square wave demodulation method is most effective.

To ensure the reliability of results, the above experiments were repeated ten times, and the average values of Vpp, CV, and SNR were calculated and summarized in Table 1.

Table 1

Comparison of demodulation effects of different methods

	square wave	sine wave	triangular wave	traditional method
Vpp(mV)	32.44	29.33	25.13	27.68
CV(%)	2.5	2.6	4.5	5.1
SNR(dB)	30.22	29.34	28.01	28.84

Compared with other demodulation schemes, the proposed square-wave demodulation yields the highest Vpp of 32.44 mV, showing a 10.06% improvement over sine-wave demodulation and a 17.22% increase over the traditional method. The variation in CV values by 2.5% confirms good repeatability. The slightly lower SNR of the traditional method is attributed to additional phase-shifting components that introduce higher noise.It is noted that the amplitude of Vpp by the square-wave demodulation signal increases by 10.06% as compared to results by the sine-wave demodulation, while it remains approximately 13.31% lower than the theoretical value. This discrepancy is likely attributed to the slight waveform distortion in the square wave demodulation generated by the AD9833 chip, leading to a certain degree of signal attenuation. Considering the sine wave as a reference signal, the output by the traditional phase-shifting demodulation method is slightly lower than that by the dual-AD9833 configuration. This is mainly due to the requirement of additional analog phase-shifting components in the traditional sine demodulation, which introduces the higher level of circuit noise.

5.2. Comparison of signal amplitudes at different MPD values

To verify the impact of the magnetic susceptibility represented by the phase φ of different metal materials on the signal demodulation of phase-locked amplifiers in practical monitoring process, the DCE method is applied to vary the MPD values. Signals are collected when monitoring metal debris with various magnetic properties and diameters.

Taking the reference signal phase as the baseline, the sensor signal phase is programmatically controlled to investigate the signal response under the consideration of different MPD values ranging from 0 to 2π with a step size of π/50. For each MPD value, the signal corresponding to each debris property is collected for 20 times, and then, the average Vpp is calculated. In the experiments, properties of metal debris considered include: 200µm iron debris, 400µm SUS304 debris, 500µm SUS316L debris, 500µm copper debris, 500µm brass debris, and 500µm aluminum debris. The calculated Vpp of all debris samples across the pre-defined MPD range of 0 to 2π are provided in Figure 10:

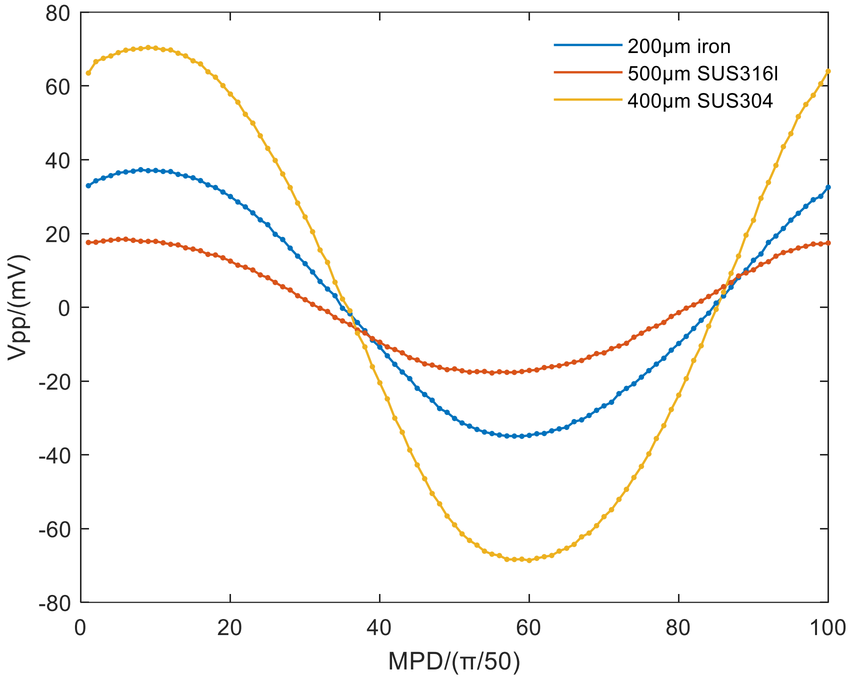

a) MPD-Vpp Curves for Iron, SUS304, and SUS316L Debris

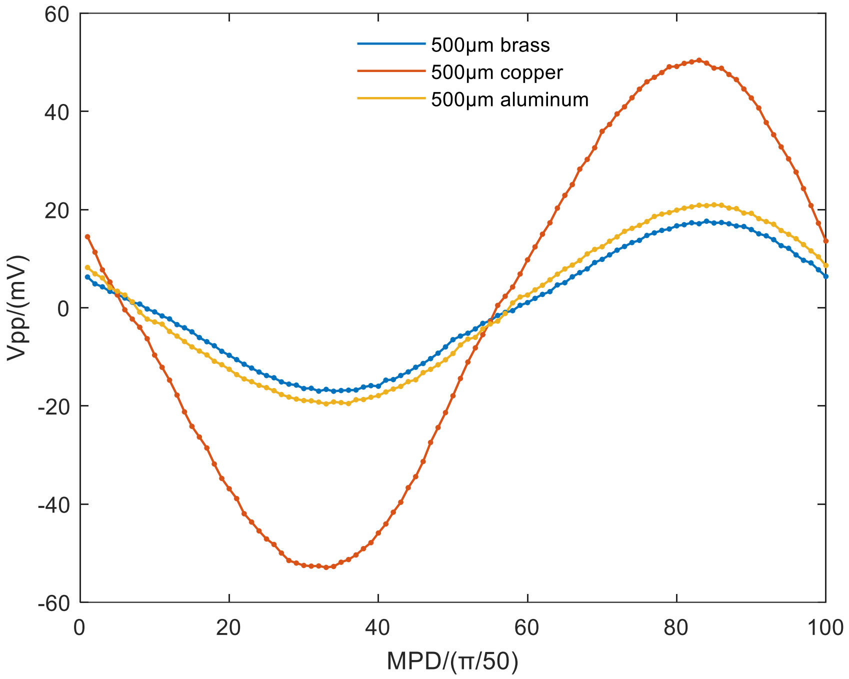

b) MPD-Vpp Curves for Copper, Brass, and Aluminum Debris

Figure 10. Vpp of Different Materials Debris at Various MPD Values

Figure 10 shows the Vpp of the monitoring signals for six types of debris with different properties across the MPD range from 0 to 2π, To ensure reliability, each data point represents the average of 20 repeated measurements. The CV for all results is below 3.5%. All signals exhibit a sinusoidal-like waveform. In Figure 10, a positive Vpp indicates that the signal's peak precedes its trough, while a negative value indicates the opposite. Due to the differences in material properties, the MPD values at which the signals reach their maximum Vpp differ significantly. The MPD value at which the demodulated signal Vpp reaches its maximum positive value is defined as the optimal MPD. When the debris signal is at the optimal MPD+π/4 (or +5π/4), the signal becomes undetectable, completely submerged in noise. This observation confirms the results from Eq. 4, Eq. 13, and the related analysis. It is also noted that Iron debris, SUS304 and SUS316l debris are able to excite good signal amplitudes at MPD values between 10π/50 and 14π/50, while copper, brass and aluminum debris achieve the remarkable amplitudes with MPD values between 81π/50 and 85π/50. Compared to the traditional method that sets the MPD to 0, the signal amplitude induced by each type of debris increases significantly, by up to 3.48 times for copper debris, 2.81 times, and 2.55 times for copper, brass, and aluminum debris, respectively. Based on the magnetic susceptibility of the debris and the phase-locked amplifier demodulation characteristics, the determination of the optimal MPD configuration for signal enhancement depends on the material property. Therefore, in practical debris monitoring, the MPD parameter should be dynamically adjusted according to the magnetic properties of the detective debris.

As indicated by Eq. 13, the signal amplitude variation rate near the optimal MPD value is small, and environmental noise from electromagnetic interference, mechanical vibrations, etc., affects the determination of the optimal MPD significantly. In contrast, the signal amplitude variation rate at the worst MPD value is large, and the phase difference of π/2 between the two is observed. This suggests that the optimal MPD value can be inferred using the MPD value in some cases where the debris signal is completely submerged in noise. To verify this conclusion, the following experiment is designed: 500μm aluminum, copper, and brass debris are spaced 200mm apart and fixed to the same nylon rope. Signals are collected at specific MPD values, with the results shown in Figure 11.

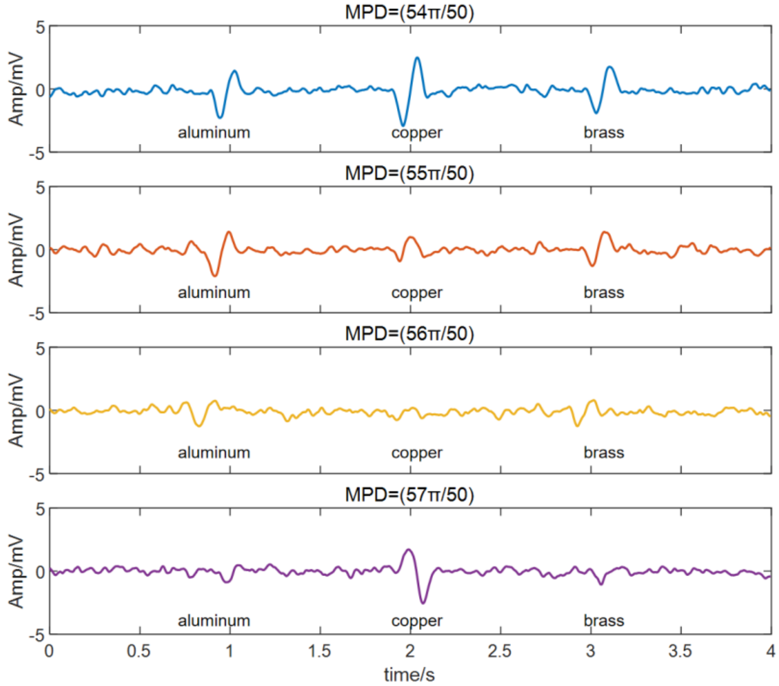

Figure 11. Signals Obtained from Copper, Brass, and Aluminum Debris at Selected MPD Values

It is observed in Figure 11 that the copper debris signal initially has an amplitude higher than those by the aluminum and brass debris, then lower, and again higher over the range of 54π/50 to 57π/50 for MPD. When the MPD value is equal to 56π/50, the copper debris signal is submerged in noise and the optimal MPD for copper is 81π/50, which is inferred by the addition of π/2 to 56π/50. The purpose of fixing the aluminum and brass debris at both ends of the copper debris is twofold: First, to mark the position of the copper debris signal; and Second, to demonstrate that the MPD values for aluminum, copper, and brass have slight differences. This observation also applies to the iron and SUS304 debris. Using this method, the optimal MPD values for the six types of debris used in the experiment are listed in Table 2.

Table 2

Optimal MPD for Different Debris

	component	size/μm	magnetic	optimal MPD
SUS316l	Austenitic structure doped with nickel and chromium	400	Weak ferromagnetism	6π/50
SUS304		500		10π/50
iron	99.9% or more iron	200	ferromagnetism	9π/50
aluminum	99.9% or more aluminum	500	paramagnetism	83π/50

copper	99.9% or more copper	500	diamagnetism	81π/50
brass	Copper-Zinc alloys	500		83π/50

The significant material-dependent differences in the optimal MPD observed in Table 2 can be explained from the perspective of the magnetic properties of metallic debris and the signal demodulation process. Under the alternating magnetic field of the inductive sensor, different debris exhibit considerable differences in complex magnetic susceptibility. Therefore, the corresponding magnetic susceptibility phase angle $\angle\chi_a$ in Eq. 9 also varies significantly. According to Eq. 13, the demodulation performance is best when the reference signal phase φ_r is adjusted to match the $\angle\chi_a$. However, due to the very short residence time of debris passing through the sensor, the $\angle\chi_a$ of debris cannot be directly measured. Thus, it can only be determined by adjusting the phase difference between the reference signal and the sensor signal without debris, while determining the φ_r by observing the optimal output.

the significant difference in optimal MPD values for different metallic materials is primarily attributed to the relationship between the real and imaginary parts of the complex magnetic susceptibility $\chi_a=\chi_a'+j\chi_a''$. The real part χ_a' represents the strength of the magnetization effect, where ferromagnetic materials exhibit an in-phase response with the excitation signal, while non-ferromagnetic materials tend to exhibit an opposite-phase tendency. The imaginary part χ_a'' represents the strength of the eddy-current effect, which introduces an approximate π/2 phase lag relative to the excitation."

For ferromagnetic materials, the response is mainly dominated by magnetization effects; therefore, the optimal MPD tends to be located near 0, where the demodulated signal reaches its maximum positive Vpp. In contrast, for non-ferromagnetic materials, the response is dominated by eddy-current effects combined with the opposite-phase magnetization contribution, resulting in an effective response that leads to a minimum negative Vpp around MPD≈π/4.

Furthermore, due to the periodicity of the demodulation process, all materials exhibit a second response with identical magnitude but opposite polarity after a phase shift of π. Considering that the optimal MPD is defined as the phase difference corresponding to the maximum positive Vpp, the optimal MPD values for ferromagnetic and non-ferromagnetic debris are accordingly identified near 0 and 3π/4, respectively.

Based on the above analysis, it is concluded that each type of metallic debris exhibits a distinct optimal MPD to achieve the corresponding maximum signal response, owing to its unique characteristic of complex magnetic susceptibility. In practical monitoring applications, the optimal MPD values for different types of wear debris can be determined through preliminary calibration experiments and stored in a database. During actual operation, the appropriate optimal MPD value can be selected from the database according to the type of wear debris being monitored and then applied to the monitoring system. The system also has the ability to realize a real-time MPD adjustment through external control commands, by dynamically tuning the demodulation phase to match the optimal value for the target debris material, the sensor can achieve the maximum detection sensitivity and SNR for that specific material. In more general monitoring scenarios where multiple types of debris may coexist, multiple parallel demodulation channels can be integrated into the sensor circuit. Each channel is configured with a different preset MPD corresponding to common wear materials. By comparing the signal amplitudes obtained from different demodulation channels, the system can not only obtain high-SNR signals for each material, but also realize simultaneous material identification based on patterns of characteristic responses.

5.3. Sensor sensitivity analysis

To further evaluate the capability of the proposed method for debris monitoring, experiments for identifying detection accuracy are conducted on typical ferromagnetic material including iron debris and diamagnetic material (copper debris). Debris samples of different sizes are selected, for example, copper debris with diameters of 200μm, 300μm, 400μm, and 500μm, and iron debris with diameters of 80μm, 100μm, 120μm, and 140μm.

The experiments are divided into two groups: iron debris and copper debris, which sequentially pass through the sensor. According to the observations described in Section 5.2, it is noted that different MPD values should be set for debris with different material properties to achieve the better SNR. Therefore, in the experiments, the MPD value is set to 9π/50 for iron debris detection and 81π/50 for copper debris inspection. To ensure the reliability of results, each experiment was repeated 10 times. The typical signal waveforms obtained in the presence of copper and iron debris are shown in Figures 12 and 13, respectively.

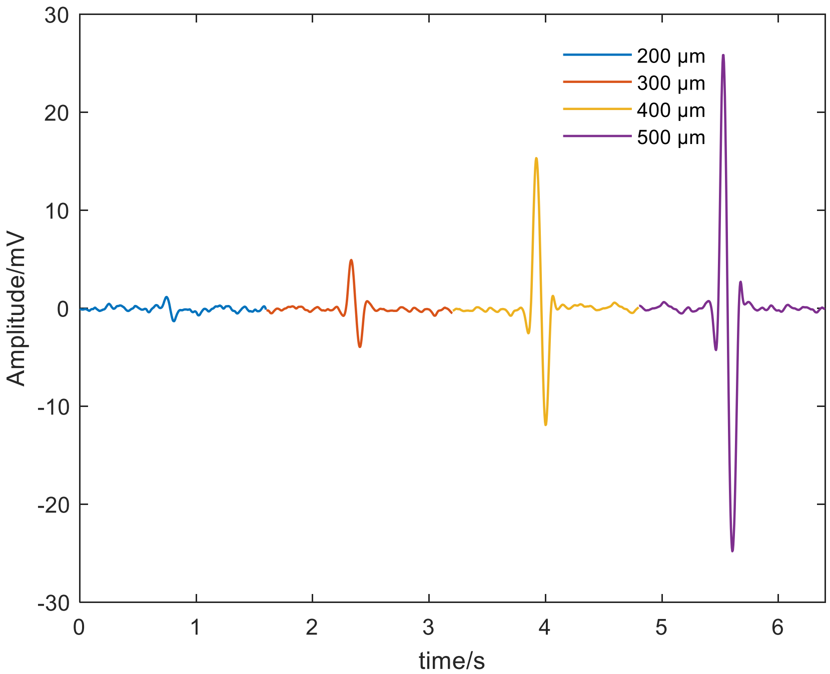

Figure 12. Signal waveforms of copper debris with different diameters

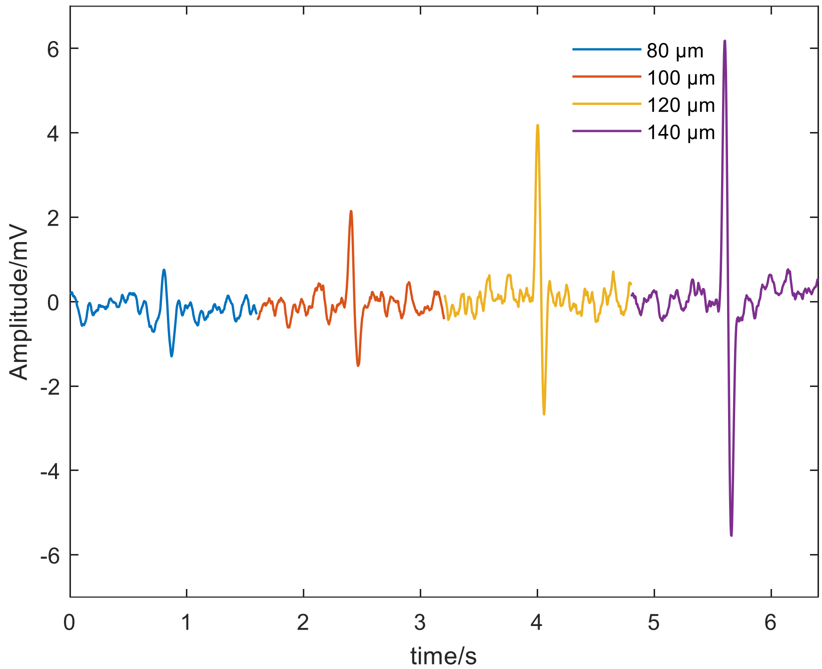

Figure 13. Signal waveforms of iron debris with different diameters

Based on 10 repeated measurements, the average value of Vpp for 200 μm copper debris is 2.46 mV, and for 80 μm iron debris is 2.05 mV. Due to the relatively low signal amplitude, the proportion of random background noise increases, leading to a higher CV by 10.5% and 9.8%, respectively. It is worth noting that the magnitudes of these two signals are slightly more than twice the baseline noise level. Therefore, 200μm and 80μm can be considered the minimum detectable diameters for copper and iron debris, respectively. Generally, under identical experimental conditions, the smaller the diameter of the sensor channel is, the smaller the minimum detectable debris size is. The sensitivity factor *S* [46] can be expressed by Eq. 15:

$$S = D_s / D_d \tag{15}$$

where D_s represents the channel diameter of the sensor, and D_d represents the minimum detectable debris diameter. A larger value of *S* indicates the better sensor performance.

According to the results obtained using Eq. 15, the proposed sensor achieves sensitivity factors of 162.5 for ferromagnetic iron debris and 65 for diamagnetic copper debris. In comparison, the existing inductive sensors described in Section Introduction typically exhibit sensitivity values in the range of 20–35 for iron debris and 6–10 for copper debris. These remarkable improvements indicate that the proposed system provides significantly enhanced overall detection performance, particularly for detecting non-ferromagnetic wear debris, while maintaining the high sensitivity of detections even for a 13mm large-diameter pipeline. The numerical quantitative comparison with existing research results is shown in Table 3:

Table 3

Comparison of results from different methods

Reference	Pipe diameter (mm)	Minimum detectable iron debris (μm)/Sensitivity factor S	Minimum detectable copper debris (μm)/Sensitivity factor S	Core technical features
Li et al. [30]	1.0	50/20.0	105/9.5	Planar coil design for improved resolution
Ma et al. [31]	0.5	20/25.0	60/8.3	Inductance-impedance correlation model
Zeng et al. [32]	0.9	33/27.3	90/10.0	Silicon steel sheet magnetic field optimization
Shen et al. [33]	3.0	93.5/32.1	447.3/6.7	Orthogonal experiment, coherent demodulation
This work	13.0	80/162.5	200/65.0	Dual-chip excitation, tunable MPD, square wave demodulation

From Table 3, it can be observed that, compared with existing approaches, the proposed method achieves a 5–10times improvement in detection sensitivity. In addition, the larger channel diameter enables operation under higher oil flow conditions, making the method more suitable for practical applications.

6. Conclusion

Inductive debris sensors currently encounter two primary challenges during the LIA process. First, traditional mixing techniques involve complicated adjustment of the reference and demodulation signals, making the process time-consuming and highly vulnerable to external interference. Second, conventional monitoring methods typically set the value of zero to the MPD, which is effective for detecting ferromagnetic debris such as iron, but may lead to the omission of diamagnetic debris. To address these limitations, this study proposes a DCE approach, which enables compact circuit integration and facilitates rapid phase adjustment of the reference signal via a MCU. Moreover, a square-wave reference signal is introduced to enhance the signal amplitude. Compared with traditional techniques, this method improves the Vpp by 19.11%. Furthermore, the study explores the application of DCE-based phase modulation for capturing signals of debris with varying magnetic properties. The experimental results indicate that the optimal MPD value for achieving the maximum signal amplitude depends on the material properties. Compared to the traditional method of setting the MPD to 0, adjusting the MPD according to the monitored debris type significantly improves the signal amplitude. As a typical example, when the MPD is properly adjusted, the signal amplitude for copper debris is increased by 3.48 times. Ultimately, the proposed sensor is capable of detecting copper debris down to

200μm and iron debris as small as 80μm in a 13mm diameter pipe system. Its corresponding sensitivity factors are 65 for copper and 162.5 for iron.

This work provides a practical solution for optimizing the LIA circuitry, reducing system complexity, while enhancing signal amplitude. For material magnetism, it introduces a novel strategy to achieve high-quality debris signals by tailoring MPD settings and lays a solid foundation for high-precision monitoring of wear debris with diverse magnetic characteristics in various industrial environments.

Appendix

Appendix Table A

Variable Explanation

Symbol	Physical meaning	Unit	Appearing Equations
$B(x,t)$	Total axial magnetic flux density in the sensor	T	(1)
B_L, B_R	Magnetic flux density generated by left and right excitation coils	T	(1), (2)
I	Amplitude of excitation current	A	(1), (2)
ω	Angular frequency of excitation current	rad/s	(1), (3), (9)
μ_0	Permeability of free space	H/m	(2), (3), (5)
n_e	Number of turns per unit length of excitation coil	turns/m	(1), (2)
$G_e(x)$	Geometric function of excitation coil set	-	(1), (6), (9)
t	Time	s	(1), (8), (10)
l_e	Length of single excitation coil	m	(2)
Re	Radius of excitation coil	m	(2)
B_{cL}, B_{cR}	Axial center positions of left and right excitation coils	m	(2)
d	Spacing between excitation coil and induction coil	m	(2), (7)
r_a	Radius of spherical metallic debris	m	(3), (6), (9)
$\mathbf{m}$	Magnetic dipole moment of magnetized debris	$A \cdot m^2$	(3), (5)
χ_a	Complex magnetic susceptibility of metallic debris	-	(3), (4), (9)
H	Intensity of applied alternating magnetic field	A/m	(3)
χ'	Real part of complex magnetic susceptibility	-	(4)
χ''	Imaginary part of complex magnetic susceptibility	-	(4)

Symbol	Physical meaning	Unit	Appearing Equations
$\angle\chi_a$	Phase angle of complex magnetic susceptibility	rad	(4), (6), (9), (13)
B_d	Magnetic dipole field generated by magnetized debris	T	(5)
r	Distance between magnetic dipole and observation point	m	(5)
$\vec{r}$	Unit vector pointing from dipole to observation point	-	(5)
Φ	Total magnetic flux induced in the induction coil	Wb	(6), (8)
$G_i(x)$	Geometric function of induction coil	-	(6), (7), (9)
l_i	Length of induction coil	m	(7)
n_i	Number of turns per unit length of induction coil	turns/m	(7)
R_i	Radius of induction coil	m	(7)
$\varepsilon(t)$	Induced electromotive force in the induction coil	V	(8), (9)
x	Axial position of debris in the sensor	m	(1), (6), (8)
v	Movement speed of debris	m/s	(8)
f_e	Frequency of excitation signal	Hz	(9)
$A(t)$	Modulation envelope of the induced signal	V	(9), (13)
ϕ_r	Phase of reference signal	rad	(10), (13)
A_r	Amplitude of reference signal	V	(10), (13)
Ms, Mq, Mt	Demodulated signal amplitudes using sine, square and triangular wave references	V	(13)
CV	Coefficient of variation of experimental data	-	(14)
SD	Standard deviation of repeated measured data	V	(14)
$\overline{A}$	Average value of measured signal amplitude	V	(14)
Ds	Channel diameter of the sensor	mm	(15)
Dd	Minimum detectable debris diameter	µm	(15)
S	Sensitivity factor of the sensor	-	(15)

Appendix Table B
Explanation and Source of Formula Meaning

Equation	Equation Meaning	Equation Source
(1)	Describes the superposition of axial magnetic fields generated by two reverse-parallel excitation coils, forming the basic excitation field of the sensor	Original derivation of this work
(2)	Calculates the axial magnetic field distribution of a single solenoid excitation coil, which is the basis for deriving the total excitation field	Original derivation of this work
(3)	Defines the magnetic dipole moment of a small spherical metallic debris magnetized in an alternating magnetic field	Cited from references [43]
(4)	Presents the complex magnetic susceptibility model of metallic materials, describing both the amplitude and phase characteristics of magnetization response	Cited from references [44]
(5)	Describes the spatial distribution of the magnetic field generated by a magnetic dipole in free space	Cited from references[43]
(6)	Calculates the total magnetic flux induced in the multi-turn induction coil by the magnetized wear debris	Original derivation of this work
(7)	Defines the geometric function of the induction coil, describing its spatial sensitivity distribution	Original derivation of this work
(8)	Faraday's law of electromagnetic induction, the fundamental physical principle underlying inductive sensing	Fundamental physical law
(9)	Core signal model of this work: approximate expression of the induced electromotive force, obtained by neglecting small velocity-dependent terms through order-of-magnitude analysis	Original derivation of this work
(10)	Defines the sine wave reference signal used in traditional lock-in amplification demodulation	Original definition of this work
(11)	Fourier series expansion of the square wave reference signal, used to analyze the demodulation performance of square wave references	Fundamental mathematical formula
(12)	Fourier series expansion of the triangular wave reference signal, used for comparative analysis of demodulation performance	Fundamental mathematical formula
(13)	Derives the demodulated output amplitudes of lock-in amplifiers using sine, square, and triangular wave references, revealing the quantitative relationship between mixing phase difference (MPD) and signal amplitude	Original derivation of this work
(14)	Defines the coefficient of variation, a statistical metric used to evaluate the dispersion and repeatability of experimental data	Standard statistical formula

Equation	Equation Meaning	Equation Source
(15)	Defines the sensitivity factor, a standardized metric for comparing the performance of inductive debris sensors with different pipe diameters	Cited from references [49]

Acknowledgments

This research is supported by the National Key Research and Development Program of China(2023YFE0111000), National Natural Science Foundation of China (12372151, 12172171 and U24A2005), Shenzhen Science and Technology Program (JCYJ20230807142004009) Shenzhen Longhua Science and Technology Innovation Special Funding Project (Industrial Sci-Tech Innovation Center of Low-Altitude Intelligent Networking) and was partially supported by Russian Ministry of Science and Higher Education (government task #FFWZ-2025-0001)

References

[1] Yang, S., Cao, N., Yu, B., 2023. Wear debris measurement in lubricating oil based on inductive method: A review. Meas. Control. 56, 1423–1434. https://doi.org/10.1177/00202940231159117.

[2] Ke, F., Ji, J.C., Qing, N., et al., 2023. A review of vibration-based gear wear monitoring and prediction techniques. Mech. Syst. Signal Process. 182, 109605. https://doi.org/10.1016/j.ymssp.2022.109605.

[3] Wang, X.L., Jin, H.W., Fu, Z.X., et al., 2026. A novel hybrid strategy for damage detection of wind turbine yaw bearing. Struct. Health Monit. 25, 1245–1262. https://doi.org/10.1177/14759217241295334.

[4] Jangra, D., Antil, P., Sidh, K.N., et al., 2025. Gear faults diagnosis: a comprehensive review of experimental and theoretical studies. Struct. Health Monit. https://doi.org/10.1177/14759217251324698.

[5] Liu, T., Sheng, H., Jin, Z., et al., 2023. A high-confidence intelligent measurement method for aero-engine oil debris based on improved variational mode decomposition denoising. Aerospace 10, 826. https://doi.org/10.3390/aerospace10100826.

[6] Li, D., Jiang, Z., 2012. Parallel sensing of metallic wear debris in lubricants using undersampling data processing. Tribol. Int. 53, 56–61. https://doi.org/10.1016/j.triboint.2012.04.005.

[7] Chen, B.Z., Zhang, H.P., Wang, W.Q., et al., 2020. Inductive-capacitive dual-mode oil detection sensor based on magnetic nanoparticle material. IEEE Sens. J. https://doi.org/10.1109/JSEN.2020.2985021.

[8] Zhu, X., Zhong, C., Zhe, J., 2017. Lubricating oil conditioning sensors for online machine health monitoring – A review. Tribol. Int. 109, 473–484. https://doi.org/10.1016/j.triboint.2017.01.015.

[9] Cao, W., Zhang, H., Wang, N., et al., 2019. The gearbox wear state monitoring and evaluation based on on-line wear debris features. Wear 426–427, 1452–1461. https://doi.org/10.1016/j.wear.2018.12.068.

[10] Guo, J., Huang, S., Wu, R., et al., 2020. A method to calculate the life of sliding bearings based on fatigue and wear failure considering fluid lubrication. J. Phys.: Conf. Ser. 1633, 012044. https://doi.org/10.1088/1742-6596/1633/1/012044.
[11] Wang, P., Li, D., Zhang, N., 2021. Research on early warning of rolling bearing wear failure based on empirical mode decomposition. Int. J. Mater. Prod. Technol. 63, 215–230. https://doi.org/10.1504/ijmpt.2021.117036.
[12] Yu, B., Cao, N., Zhang, T., 2021. A novel signature extracting approach for inductive oil debris sensors based on symplectic geometry mode decomposition. Measurement 185, 110056. https://doi.org/10.1016/j.measurement.2021.110056.
[13] Luan, X.C., Zhao, J.H., Sha, Y.D., et al., 2025. Rolling bearing state monitoring method based on fusion of multichannel vibration signals with oil debris information. Struct. Health Monit. https://doi.org/10.1177/14759217241301305.
[14] Song, F., Zhou, Q.H., Fu, B., et al., 2021. Wear debris segmentation of reflection ferrograms using lightweight residual U-Net. IEEE Trans. Instrum. Meas. 70, 1–10. https://doi.org/10.1109/TIM.2021.3099573.
[15] Dai, X., Wang, Y., Yu, S., 2017. Ferrographic analysis of pivot jewel bearing in oil-bath lubrication. Wear 376–377, 1089–1096. https://doi.org/10.1016/j.wear.2017.02.001.
[16] He, Y., Li, M., Meng, Z., et al., 2021. An overview of acoustic emission inspection and monitoring technology in the key components of renewable energy systems. Mech. Syst. Signal Process. 148, 110146. https://doi.org/10.1016/j.ymssp.2020.107146.
[17] Feng, S., Zhang, J., Fan, B., et al., 2023. A panoramic ferrograph for on-site detection of oil wear debris. Tribol. Int. 190, 109035. https://doi.org/10.1016/j.triboint.2023.109025.
[18] Liu, Z., Liu, Y., Zuo, H., 2022. Oil debris and viscosity monitoring using optical measurement based on response surface methodology. Measurement 195, 111152. https://doi.org/10.1016/j.measurement.2022.111152.
[19] Qian, M., Ren, Y., Feng, Z., 2022. Wear debris sensor using intermittent excitation for high sensitivity, wide detectable size range, and low heat generation. IEEE Trans. Ind. Electron. 70, 9382–9391. https://doi.org/10.1109/TIE.2022.3190894.
[20] Liu, Z., Wang, J., Liu, Y., et al., 2025. A new MRCAHE method for wear particle image enhancement based on improved online optical microfluidic sensor. Tribol. Lett. 73, 55. https://doi.org/10.11249/025-01994-1.
[21] Sun, J., Wang, L., Li, J., et al., 2021. Online oil debris monitoring of rotating machinery: A detailed review of more than three decades. Mech. Syst. Signal Process. 149, 110141. https://doi.org/10.1016/j.ymssp.2020.107341.
[22] Han, Z., Wang, Y., Qing, X., 2017. Characteristics study of in-situ capacitive sensor for monitoring lubrication oil debris. Sensors 17, 2851. https://doi.org/10.3390/s17122851.
[23] Zhu, L., Xiao, X., Wu, D., et al., 2022. Qualitative classification of lubricating oil wear particle morphology based on coaxial capacitive sensing network and SVM. Sensors 22, 6539. https://doi.org/10.3390/s22176653.

[24] Zhang, Y., Sun, Y., Wen, Y., 2021. An imaging algorithm of planar array capacitance sensor for defect detection. Measurement 168, 108456. https://doi.org/10.1016/j.measurement.2020.108466.
[25] Iwai, Y., Honda, T., Miyajima, T., et al., 2010. Quantitative estimation of wear amounts by real time measurement of wear debris in lubricating oil. Tribol. Int. 43, 623–629. https://doi.org/10.1016/j.triboint.2009.06.019.
[26] Xu, C., Zhang, P., Wang, H., et al., 2015. Ultrasonic echo waveshape features extraction based on QPSO-matching pursuit for online wear debris discrimination. Mech. Syst. Signal Process. 60, 301–315. https://doi.org/10.1016/j.ymssp.2015.01.002.
[27] Zeng, L., Zhang, H., Wang, Q., 2018. Monitoring of non-ferrous wear debris in hydraulic oil by detecting the equivalent resistance of inductive sensors. Micromachines 9, 127. https://doi.org/10.3390/mi9030117.
[28] Fang, Y., Nie, Y., Du, Y., 2025. An improved high-throughput imaging sensor for macroscale and microscale features of wear particles in online condition monitoring. IEEE Sens. J. 25, 7892–7901. https://doi.org/10.1109/JSEN.2024.3513643.
[29] Yin, Y.B., Zhang, Q., Feng, L., 2023. A wear debris recognition method based on dual-channel electrostatic signal and prominence of cross-correlation function. Tribol. Int. 190, 109020. https://doi.org/10.1016/j.triboint.2023.109020.
[30] Li, D., Jiang, Z., 2011. A high throughput inductive pulse sensor for online oil debris monitoring. Tribol. Int. 44, 175–181. https://doi.org/10.1016/j.triboint.2010.10.022.
[31] Ma, L., Shi, H., Zhang, H., et al., 2020. High-sensitivity distinguishing and detection method for wear debris in oil of marine machinery. Ocean Eng. 215, 107452. https://doi.org/10.1016/j.oceaneng.2020.107452.
[32] Zeng, L., Yu, Z., Zhang, H., et al., 2018. A high sensitive multi-parameter micro sensor for the detection of multi-contamination in hydraulic oil. Sens. Actuators A Phys. 282, 201–210. https://doi.org/10.1016/j.sna.2018.09.023.
[33] Shen, X., Han, Q., Wang, Y., 2023. Research on detection performance of four-coil inductive debris sensor. IEEE Sens. J. 23, 15678–15687. https://doi.org/10.1109/JSEN.2023.3249215.
[34] Wu, X., Zhang, Y., Li, N., et al., 2021. A new inductive debris sensor based on dual-excitation coils and dual-sensing coils for online debris monitoring. Sensors 21, 7566. https://doi.org/10.3390/s21227556.
[35] Bai, C., Zhang, H., Zeng, L., et al., 2020. Inductive magnetic nanoparticle sensor based on microfluidic chip oil detection technology. Micromachines 11, 926. https://doi.org/10.3390/mi11020183.
[36] Behbahani, K.M., Aliyu, A., Bishop, D.P., et al., 2024. Additive manufacturing of copper-based alloys for high-temperature aerospace applications: A review. Mater. Today Commun. 38, 108679. https://doi.org/10.1016/j.matcomm.2024.108679.
[37] Mochugovskiy, A.G., Mikhaylovskaya, A.V., 2020. Comparison of precipitation kinetics and mechanical properties in Zr and Sc-bearing aluminum-based alloys. Mater. Lett. 275, 128096. https://doi.org/10.1016/j.matlet.2020.128096.

[38] Al-Othman, M.A., Gani, K.E., Daud, K.A., et al., 2022. Bearing aluminum-based alloys: Microstructure, mechanical characterizations, and experiment-based modeling approach. Materials 15, 7985. https://doi.org/10.3390/ma15238394.
[39] Wu, Q., Pan, F., Wang, L., et al., 2024. Frictional wear behavior of water-lubrication resin matrix composites under low speed and heavy load conditions. Polymers 16, 1927. https://doi.org/10.3390/polym16192753.
[40] Lin, C.-L., Meehan, P.A., 2021. Morphological and elemental analysis of wear debris naturally formed in grease lubricated railway axle bearings. Wear 484–485, 203994. https://doi.org/10.1016/j.wear.2021.203994.
[41] Su, L.J., Wang, F.M., Song, W., et al., 2022. Effect of heat treatment processes on the microstructure and mechanical properties of low alloy structural steels with different impurity tin contents. Ironmak. Steelmak. 49, 689–697. https://doi.org/10.1080/03019233.2021.2014169.
[42] Perfilyev, V., Moshkovich, A., Lapsker, I., et al., 2010. Friction and wear of copper samples in the steady friction state. Tribol. Int. 43, 987–994. https://doi.org/10.1016/j.triboint.2010.01.022.
[43] Griffiths, D.J., 1999. Introduction to Electrodynamics. Prentice Hall, New Jersey.
[44] Zou, X.M., Zhang, L., Zhang, H.P., et al., 2019. Magnetization model and detection mechanism of a microparticle in a harmonic magnetic field. IEEE/ASME Trans. Mechatron. 24, 2568–2577. https://doi.org/10.1109/TMECH.2019.2928704.
[45] Ren, Y.J., Wen, X.L., Gao, S.W., et al., 2023. Theoretical and simulation analysis on the spatial resolution of magnetic metal debris sensors. Front. Mater. 10, 1110834. https://doi.org/10.3390/fmats.2023.1110834.
[46] Zhang, M., 2024. Short-time variance providing evidential reference frequency for lock-in amplifier in fault diagnosis of rolling bearings. J. Vib. Eng. Technol. 12(2), 567–578. https://doi.org/10.1007/s42417-024-01508-8.
[47] Algueta-Miguel, J.M., Beato-Lopez, J.J., Lopez-Martin, A.J., et al., 2024. A lock-in amplifier for magnetic nanoparticle detection using GMI sensors. IEEE Trans. Instrum. Meas. 73, 1–10. https://doi.org/10.1109/tim.2024.3470988.
[48] Li, R., Ouyang, H., Liu, H., 2025. A novel digital lock-in amplifier with extended Lyapunov demodulation for wide dynamic range applications. IEEE Trans. Instrum. Meas. 74, 1–9. https://doi.org/10.1109/tim.2025.3595634.
[49] Ren, Y.J., Li, W., Zhao, G.F., et al., 2018. Inductive debris sensor using one energizing coil with multiple sensing coils for sensitivity improvement and high throughput. Tribol. Int. 128, 56–65. https://doi.org/10.1016/j.triboint.2018.07.025.